Modeling and Parametric Study of a Single Solid Oxide Fuel Cell by Finite Element Method

K. Daneshvar[1]*, G. Dotelli[1], C. Cristiani[1], R. Pelosato[1], M. Santarelli[2]

[1] Politecnico di Milano, Dipartimento di Chimica, Materiali e Ingegneria Chimica "G. Natta", and INSTM R.U. Polimi, p.zza L. da Vinci 32, 20133, Milano, Italy

[2] Politecnico di Torino, Dipartimento di Energetica, Torino 10129, Italy

Received October 25, 2013; accepted January 09, 2014; published online February 21, 2014

1 Introduction

Solid oxide fuel cells (SOFCs) are electrochemical devices that can efficiently convert chemical energy into electrical energy. Compared to other types of fuel cells, they are characterized by their high working temperature, typically between 800 and 1,000 °C: this also represents the largest disadvantage, due to increasing costs and longer start-up times; anyway, in this way SOFCs do not require an expensive platinum catalyst as is currently necessary for lower temperature fuel cells. Moreover, using new kind of electrolytes the working temperature of SOFCs could be decreased to 600–800 °C to have less disadvantages in comparison with high temperature ones. Research in this field is ongoing to affirm this technology as a viable energy alternative. SOFCs are characterized by a solid oxide electrolyte to conduct negative oxygen ions from the cathode to the anode: the most used material is Yttria-Stabilized Zirconia ($Zr_{1-x}Y_xO_{2-\delta}$, YSZ). The electrodes are solid oxides too: the anode, where the electrochemical oxidation of hydrogen occurs, is a cermet made up of Nickel and YSZ (Ni–YSZ); the cathode, where oxygen reduction takes place, is a composite of Strontium-doped Lanthanum manganite ($La_{1-x}Sr_xMnO_{3-\delta}$, LSM) and YSZ [1–3].

Modeling and computer simulation are gaining increasing popularity as they are used for studying the condition of hypothetically functioning systems without them being actually constructed, and solving possible problems at this stage with an obvious saving of time and costs. Hence, mathematical problem solving techniques have been developed for bringing the constructed models to an optimal condition. Therefore, computational modeling plays an important role in order to expand the potential and reduce the disadvantages [4–9].

There are plenty of papers in the literature in which model validation is against literature data [5, 6, 10]; of course, the availability of experimental data to compare with allows a direct knowledge of the cell characteristics and operating conditions, so the model behavior can be evaluated much better. This is the approach that the authors pursued in the present

[*] *Corresponding author, keyvan.daneshvar@polimi.it*

paper, as it is often of great advantage in the model development, like in Xie and Xure [7].

Different examples of SOFC modeling can be found in the literature: Janardhanan and Deutschmann [5] used a computational approach with a detailed multi-step model for heterogeneous chemistry in the anode, modified Butler–Volmer formalism for the electrochemistry and Dusty Gas Model (DGM) for the porous media transport; the model equations have been solved for a button cell configuration. Their study focused on the chemical and electrochemical process in an internally reforming anode supported SOFC button cell running on humidified CH_4, and they could conclude that using direct internal reforming results in an increased overall efficiency of the system.

Other authors also included heat transfer simulation in their modeling [6, 10]. Barzi et al. [6] simulated the electrical and electrochemical processes in a button cell, and they found a 9 °C maximum temperature variation in the cell body at 10,000 A m^{-2} at 1,073 K.

Even more complex modeling is possible, as in the paper by Xie and Xue [7]: the authors performed extensive simulations to elucidate the complex interactions between fuel/gas species, adsorbed/desorbed surface ions, elementary reactions, and their effects on the cell performance.

In this work, a 2D isothermal axisymmetric model of an anode-supported SOFC single cell has been developed and validated against experimental data obtained on a Ni–YSZ/YSZ/LSM–YSZ cell [11, 12]; COMSOL Multi-physics 4.3a was used for this work, as it is a flexible tool able to manage different physical approaches.

The developed model includes the following processes: electronic and ionic charge balance (Ohm's law), Butler–Volmer charge transfer kinetics, flow distribution in gas channels (Navier–Stokes), flow in the porous gas diffusion electrodes (GDEs) (Brinkman equations), gas phase mass balances in both fuel and air channels, and in porous electrodes (Maxwell–Stefan diffusion and convection). Heat transfer simulation has not included in the model at this stage; given the small size of the cell, temperature gradients [6] are not expected to significantly affect the simulation results.

In addition, a parametric analysis has been done to evaluate the effect of some important parameters, such as material properties, geometric features and temperature, on the cell performance. This is one of the biggest advantages of the simulation compared to experimental methods, where the change of specific parameters and the geometry would require a significant amount of costs and time.

2 Model Setup and Methods

SOFCs could have different geometries (planar, tubular, and monolithic); laboratory scale experiments usually adopt anode-supported circular–planar cells, the so-called button cell, which is used in this study as well. In anode-supported cells the anode is the thickest and strongest layer, providing the mechanical support.

2.1 Cell Description

In Figure 1, a scanning electron microscope (SEM) image of a section of the SOFC is reported. The radius of the cell is 40 mm, while the thickness of the anode, electrolyte and cathode are 540, 6, and 36 μm, respectively. The anode is made of two different layers: starting from the bottom of Figure 1, there are the support layer (534 μm, Ni–YSZ cermet with 30% YSZ) and the active layer (6 μm, Ni–YSZ cermet with 50% YSZ). In the cathode side, starting from the top of Figure 1, there finds the current collector layer (20 μm, 100% LSM) and the active layer (16 μm, 50:50 LSM–YSZ composite) [11]. The 6 μm thick dense YSZ electrolyte is in the middle.

2.2 Model Description

The cell to be simulated has an axisymmetrical geometry, hence it is possible to choose 2D instead of 3D geometry. Indeed, applying a rotation through the axis of symmetry, a 3D geometry is obtained. This allows easier and faster calculations. The geometry of the cell was built in strict agreement with the actual cell geometry; five layers were adopted in the geometry to replicate the actual microstructure of the cell [11]. The geometry of feeding system is the same for fuel and oxidant, and each one is composed by two concentric channels, one inside the other: hydrogen and air enter from the inner channel towards to center of the cell, and the reaction products come out through the outer channel; in Figure 2a the geometry of the cell and in Figure 2b the whole geometry of the system is reported with its mesh built. The radius of the inner channel is 14 mm with a wall thickness of 2 mm.The distance between the outlet of inner channels and the electrodes (standoff distance) is 20 mm.

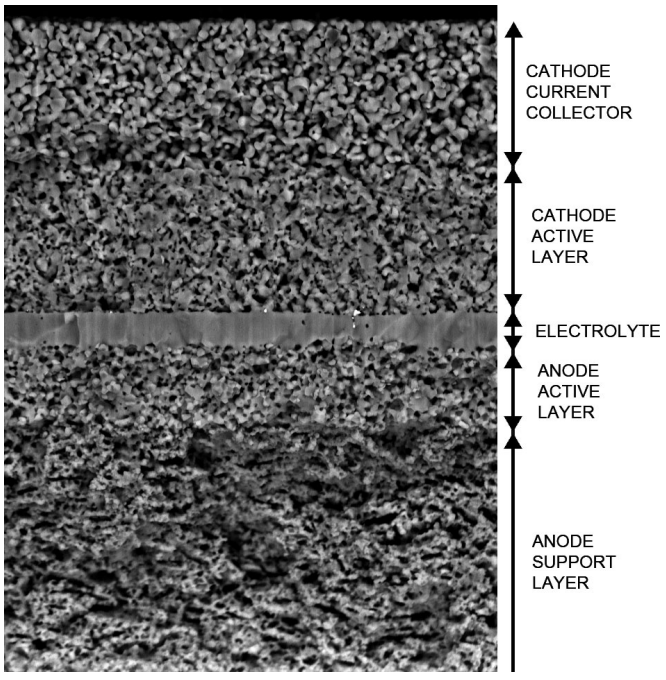

Fig. 1 SEM micrograph of a section of the cell.

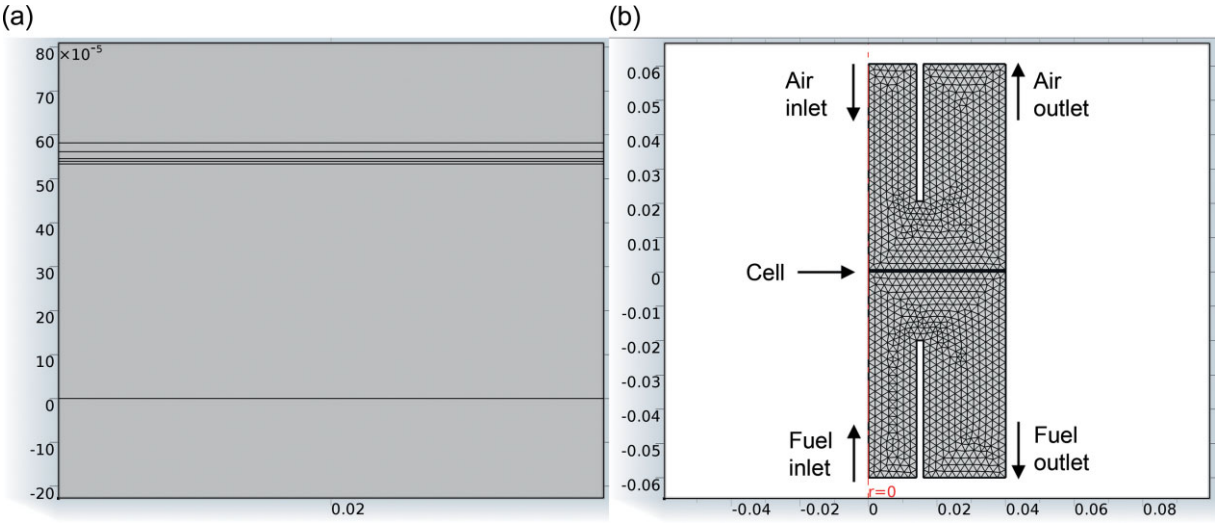

Fig. 2 (a) configuration of the cell from bottom to up: anode support, anode active area, electrolyte, cathode active area and cathode current collector and (b) Axisymmetric meshed geometry of the whole setup; cell size is in m.

Sufficiently fine free triangular mesh has been used for the fuel and air channels and a mapped mesh has been used for the cell, distributed to cover all the parts of the cell. The complete mesh of the setup consists of 7,745 elements. In different layers of the cell, depending on the importance of the layer and on required computation accuracy, different fixed numbers of elements have been used: 100 elements in anode, 25 elements in electrolyte and 50 elements in cathode have been applied. Based on the mesh refinement and statistical analysis done on all domains, this choice ensures a good accuracy and no dependency of the results on the computational grid.

In the present model these features were used: (i) the Secondary Current Distribution interface for the electronic and ionic charge balance in the anode, electrolyte and cathode; (ii) Transport of Concentrated Species interface for the diffusion in the electrodes and their respective feeders; (iii) Free and Porous Media Flow interface for the velocity and pressure fields linked to the fuel and air gases.

After building the cell geometry, it is then necessary to decide which mathematical approaches should be used. In particular, in this work these kinds of modeling have been chosen: Ohm's law for the electronic and ionic charge balance, Butler–Volmer kinetics for the charge transfer, Navier–Stokes equations for the flow distribution in the gas channels, Brinkman equations for the flow in the porous gas distribution electrodes and Maxwell-Stefan diffusion and convection for the mass balances in gas phase in both gas channels and porous electrodes.

In order to simplify the computation, several assumptions are considered and applied: (i) the fuel cell operates under steady-state conditions; (ii) reactant species are compressible ideal gases; (iii) the flow in the channels is laminar; (iv) the electrolyte is impermeable to reactant gases; (v) materials are isotropic and homogenous; (vi) their chemical and physical properties are constant in time with no degradation [4, 5, 7, 11, 13].

Details about cell parameters, materials properties, and operating conditions are reported in Table 1. Regarding the physical parameters that were not experimentally available, the authors tried to stick as much as possible to physically sound values, to avoid using these parameters as 'fitting factors' for the model validation.

2.3 Governing Equations

2.3.1 Charge Balance

Charge balance including the ionic and electronic transports were studied here based on Ohm's law. The general equation is according to the following [14, 15]:

$$\nabla i_k = Q_k \tag{1}$$

$$\phi_k = -\sigma_k \nabla \Phi_k \tag{2}$$

Q_k is a general source term where k denotes an index that is l for the electrolyte or s for the electrode, in A m^{-3}, σ_k is the conductivity in S m^{-1} and Φ_k the potential in V.

The charge balances in the electrolyte and in the electrode matrix contain sources and sinks according to the charge transfer reaction that takes place in the electrode catalyst. For example, if the porous electrode is a cathode, then the charge transfer reaction is a source for the charge balance in the electrode, since it receives current from the electrolyte. The charge transfer reaction is then a sink for the charge balance in the electrolyte, since the current is transferred from the electrolyte to the electrode in a cathodic reaction [16].

The electrodes of the cell are composites of an ionic conducting phase (YSZ) and an electronic conducting one (Ni in the anode, LSM in the cathode); therefore, in the electrodes ionic and electronic transports coexist. The effective electronic and ionic conductivities have been evaluated by the following expressions [7]:

Table 1 Material properties and operating conditions used in the simulation [5, 8, 11, 12, 30–36]

Inputs and units	Quantities	References
Operating pressure P / Pa	101, 325	–
Inlet temperature T / K	1,073, 1,003	–
Faraday Constant F / C mol^{-1}	96,485	–
Gas constant R / J mol^{-1} K^{-1}	8.314	–
Fuel component mass fraction wt.%	0.73 H_2, 0.27 H_2O	–
Oxidant component mass fraction wt.%	0.25 O_2, 0.75 N_2	–
Anode ionic resistivity / Ω cm	(2.98×10^{-2}) exp(10,350/T)	[11, 12]
Anode electronic resistivity / Ω cm	(3.07×10^{-4}) exp(–556.34/T)	[11, 12]
Cathode electronic resistivity / Ω cm	(1.7×10^{-3}) exp(1,280/T)	[11, 12]
Electrolyte ionic conductivity / S cm^{-1}	(3.34×10^{2}) exp(–10,300/T)	[11, 12]
Anode active layer ionic resistivity / Ω cm	(7.1×10^{-3}) exp(10,350/T)	[11, 12]
Anode active layer electronic resistivity / Ω cm	(1.9×10^{-4}) exp(–556.61/T)	[11, 12]
Cathode active layer ionic resistivity / Ω cm	(7.90×10^{-3}) exp(10,350/T)	[11,12]
Cathode active layer electronic resistivity / Ω cm	(3.2×10^{-3}) exp(1279.8/T)	[11, 12]
Air mass flow / kg s^{-1}	3.2×10^{-5}	–
Fuel mass flow / kg s^{-1}	0.78×10^{-6}	–
Anode and anode functional layer porosity ε	0.2, 0.1	[11, 12]
Anode and anode functional layer permeability κ / m^2	5.76×10^{-15}, 9.83×10^{-15}	[30–32]
Cathode and cathode functional layer porosity ε	0.3, 0.2	[11, 12]
Cathode and cathode functional layer permeability κ / m^2	1.76×10^{-15}, 1.27×10^{-15}	[30–32]
Viscosity of fuel / Pa s	9.1×10^{-6}	–
Viscosity of oxidant / Pa s	17.27×10^{-6}	–
Anode exchange current density / A m^{-2}	5,300	[8]
Cathode exchange current density / A m^{-2}	2,000	[8]
Anode active specific surface area $a_{v,a}$ / m^{-1}	1.025×10^5	[5, 33]
Cathode active specific surface area $a_{v,c}$ / m^{-1}	2.025×10^5	[5, 33]
Tortuosity τ	2	[34, 35]
Average pore diameter d_{pore} / μm	1	[36]
Average particle diameter d_p / μm	2.5	[36]

$$\sigma_{e,eff} = \phi \cdot \left(\frac{(1-\varepsilon)}{\tau}\right) \cdot \sigma_e \tag{3}$$

$$\sigma_{i,eff} = (1-\phi) \cdot \left(\frac{1-\varepsilon}{\tau}\right) \cdot \sigma_i \tag{4}$$

where ϕ is the volume fraction of electronic conducting phase in the electrode, ε is the porosity of the layer, and τ is its tortuosity.

2.3.2 Charge Transfer Current Density

To describe the charge transfer current density and transport phenomena in the electrodes the Butler–Volmer formula has been used, which takes into account reactant concentrations by considering diffusion polarization. At the anode, hydrogen is oxidized to produce steam; assuming that the transfer of the first electron is the rate determining step, the charge transfer kinetics equation leading to compute anode local current density is as follows [14, 15, 17]:

$$i_a = i_{0,a}\left[\frac{c_{H_2}}{c_{H_2,ref}}\exp\left(\frac{0.5F}{RT}\eta\right) - \left(\frac{c_{H_2O}}{c_{H_2O,ref}}\right)\exp\left(\frac{-1.5F}{RT}\eta\right)\right] \tag{5}$$

where $i_{0,a}$ is the anode exchange current density in A m^{-2}, c_{H_2} is the molar concentration of hydrogen in mol m^{-3} and c_{H_2O} is the molar concentration of steam in mol m^{-3}. $c_{H_2,ref}$ and $c_{H_2O,ref}$ are the reference (input) concentrations in mol m^{-3}. F is Faraday's constant in C mol^{-1}, R the gas constant in J mol^{-1} K^{-1}, T the temperature in K, and η the overvoltage in V.

So the current density (per unit volume) in anode side is [14, 15]:

$$j_a = a_{v,a}\, i_a \tag{6}$$

where $a_{v,a}$ is anode active specific surface area in m^{-1}.

At the cathode, where oxygen acquires two electrons, the charge transfer kinetics equation leading to compute cathode local current density is the following [14, 15, 17]:

$$i_c = i_{0,c}\left[\exp\left(\frac{3.5F}{RT}\eta\right) - x_{O_2}\left(\frac{c_t}{c_{O_2,ref}}\right)\exp\left(\frac{-0.5F}{RT}\eta\right)\right] \tag{7}$$

where $i_{0,c}$ is the cathode exchange current density in A m^{-2}, $c_{O_2,ref}$ is the reference concentration of oxygen in mol m^{-3}, c_t is the total molar concentration of species in mol m^{-3} and x_{O_2} is the molar fraction of oxygen, and η the overvoltage in V.

So the current density (per unit volume) in cathode side is [14, 15]:

$$j_c = a_{v,c}\, i_c \tag{8}$$

where $a_{v,c}$ is cathode active specific surface area in m^{-1}.

The active specific surface areas represent the small fraction of the electrodes structure, which is accessible to reactant species and this term is one of the most important in electrode morphology and also strongly influences the electrodes resistance [18].

2.3.3 Transport of Concentrated Species

Gas-phase species transport is described here by the modified Maxwell–Stefan equation [19–22]:

$$\rho\frac{\partial}{\partial t}(\omega_i)+\rho(u\cdot\nabla)\omega_i=\nabla\left(\rho\omega_i\sum_{k=1}^{Q}D_{ik}d_k+D_i^{\mathrm{T}}\frac{\nabla T}{T}\right)+R_i \tag{9}$$

where ρ denotes the mixture density in kg m^{-3}, ω_i is the mass fraction of the species in the mixture and u is the mass average velocity of the mixture in m s^{-1}. D_{ik} is the multi-component effective diffusion coefficient of species i and k in m^2 s^{-1}, which includes both ordinary and Knudsen effective diffusion coefficients, and D_i^{T} is the thermal diffusion coefficient in kg m^{-1} s^{-1}. Here, the temperature gradient term is zero based on isothermal condition. Also, in a multi-component mixture, the sum of the thermal diffusion coefficients is zero. R_i is the rate expression describing production or consumption of the species. d_k is the diffusional driving force acting on species k in m^{-1}, equal to [19–22]:

$$d_k=\nabla x_k+\frac{1}{p}\left[(x_k-\omega_k)\nabla p-\rho\,\omega_k g_k+\omega_k\sum_{l=1}^{Q}\rho\omega_l g_l\right] \tag{10}$$

The molar fraction x_k is:

$$x_k=\frac{\omega_k}{M_k}M \tag{11}$$

The mean molar mass M in kg mol^{-1} is:

$$\frac{1}{M}=\sum_{i=1}^{Q}\frac{\omega_i}{M_i} \tag{12}$$

and g_k in m s^{-2} is an external force (per unit mass) acting on species k.

Bulk diffusivity of a binary gas could be evaluated by using an empirical equation based on kinetic gas theory [23]:

$$D_{ij}=\frac{3.16\cdot10^{-8}\cdot(T^{1.75})\cdot\left(\frac{1}{M_i}+\frac{1}{M_j}\right)}{p\cdot\left(V_i^{1/3}+V_j^{1/3}\right)} \tag{13}$$

where M_i and M_j in kg mol^{-1} are the molecular weights of the species and V_i and V_j in m^3 mol^{-1} are the gases diffusion volumes.

The Knudsen diffusion includes the wall collisions effect and is really important for small pore diameters and can be determined by the following expression for the gas component i and j in a gas mixture based on free molecule flow theory [24]:

$$D_{ij,Knudsen}=\frac{1}{3}d_{pore}\cdot\left(\frac{8RT}{\pi M_{ij}}\right)^{0.5} \tag{14}$$

where d_{pore} in μm is the pore diameter and M_{ij} can be computed by:

$$M_{ij}=\frac{2}{\left(\frac{1}{M_i}+\frac{1}{M_j}\right)} \tag{15}$$

Finally, to have an effective diffusion coefficient, the coefficients are usually corrected using porosity (ε) and tortuosity (τ) as in the following [24, 25]:

$$D_{ik}=D_{eff,ij}=\frac{\varepsilon}{\tau}\frac{(D_{ij}\cdot D_{ij,Knudsen})}{(D_{ij}+D_{ij,Knudsen})} \tag{16}$$

2.2.4 Flow in Channels

The flow in the channels is governed by the Navier–Stokes equations using the steady state form of continuity and conservation of momentum equations [26, 27]:

$$\nabla\cdot(\rho u)=0 \tag{17}$$

$$\rho(u\cdot\nabla)u=\nabla\cdot\left[-pI+\mu(\nabla u+(\nabla u)^T)-\frac{2}{3}(\nabla\cdot u)I\right] \tag{18}$$

where u is the gas velocity in m s^{-1}, ρ is the gas density in kg m^{-3}, p is the pressure in Pa and μ is the gas dynamic viscosity in kg m^{-1} s^{-1}.

The gas density is easily computed by applying the ideal gas law and the molar fraction of species using the following formula:

$$\rho=\frac{PM}{RT} \tag{19}$$

where M in kg mol^{-1} is the mean molar mass of the gas mixture.

2.3.5 Flow in Porous Media

In the porous gas diffusion catalyst layers, the equation changes by using the modified continuity and conservation of momentum equations [26, 27]:

$$\nabla\cdot(\rho u)=Q \tag{20}$$

$$\left(\frac{\mu}{\kappa}+Q\right)u=\nabla\cdot\left[-pI+\frac{\mu}{\varepsilon}(\nabla u+(\nabla u)^T)-\frac{2}{3}(\nabla\cdot u)I\right] \tag{21}$$

where ε is the porosity of the layer and κ is its permeability in m^2.

Equation (21) is also known as Brinkman equation. Also, the permeability can be computed using Kozeny–Carman formula [28]:

$$\kappa=\frac{(\varepsilon^3 d_p^2)}{(72\tau(1-\varepsilon)^2)} \tag{22}$$

where ε is the porosity of the layer and τ is the tortuosity. d_p in μm stands for particle diameter.

3 Results and Discussion

3.1 Model Validation

Figure 3 shows the polarization curves and the power density *versus* current density curves obtained from the modeling, compared with those obtained from experimental data [11, 12]. The choice of potential range in the simulation of polarization curves was done in accordance with available experimental data.

In Figure 3a, the comparison is shown for the cell operating at 1,073 K, 400 ml min^{-1} fuel stream; in Figure 3b the comparison is made at 1,073 K and 500 ml min^{-1} fuel stream. Air feeding was in all cases 1,500 ml min^{-1}. In the low fuel stream (Figure 3a), the experimental and model curves are perfectly superimposable through all the current density range. In the high fuel stream condition (Figure 3b) some discrepancies exist at high current densities (> 6×10^3 A m^{-2}); the validity of the model is anyway confirmed in both feeding conditions. Nevertheless, for the high fuel stream curve, disagreement in the high current density range is tentatively accounted for by the possible underestimation of the utilization factor and fuel starvation effect. The concentration of the reactants at the catalyst site are underestimated, so the mass transport model does not get the exact value of these concentrations at very high current density.

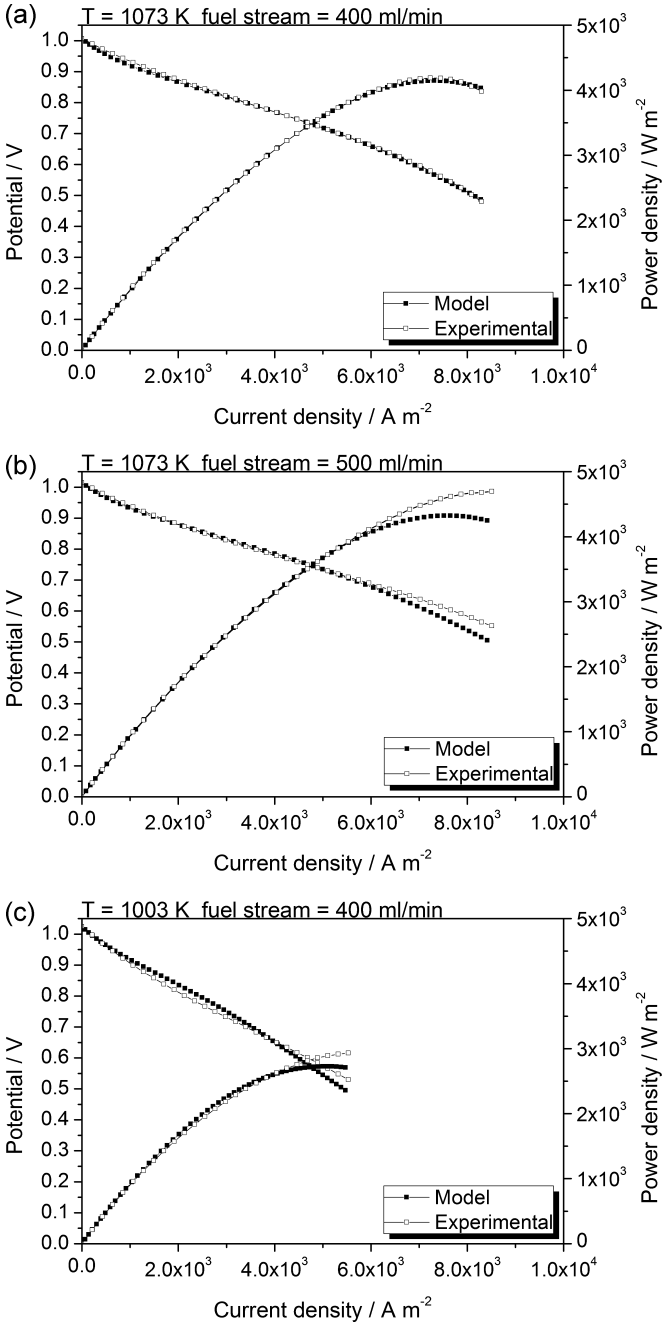

Fig. 3 Polarization and power density *versus* current density curves for cell operating at (a) 1,073 K and 400 ml min^{-1}/fuel stream; (b) 1,073 K and 500 ml min^{-1}/fuel stream; (c) 1,003 K and 400 ml min^{-1}/fuel stream.

In Figure 3c, the polarization and power density curves *versus* current density are shown with the cell operating at 1,003 K, 400 ml min^{-1} fuel stream. As expected, at lower temperature (1,003 K) both experimental data and modeling results show a decrease in the power density; of course, this is due to increasing losses with decreasing temperature. Also in this situation, the agreement between the model and the experiment is very satisfactory, with only a slight discrepancy between the model and experimental curves at the current density ranges from 1×10^3 to 3×10^3 A m^{-2} and at the very last current density points. At this stage, it is not so clear what could be the definite reason of this slight discrepancy in low-temperature condition.

3.2 Cell Potential and Current Density

Figure 4 shows the trend of the cell potential: Figure 4a illustrates the potential inside an enlarged section of the cell

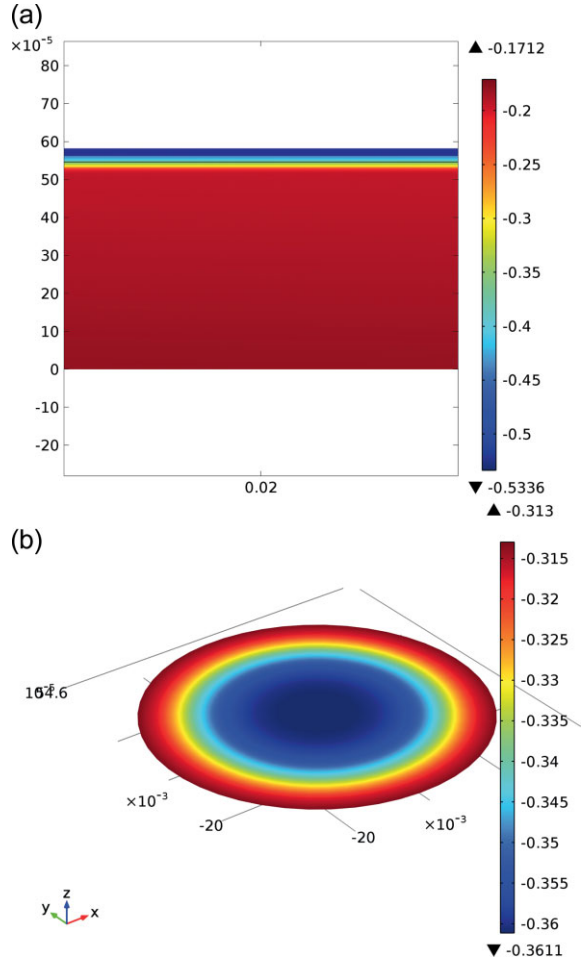

Fig. 4 (a) Side view of the cell potential/V and (b) top view of the cell potential/V at electrolyte-cathode interface at 0.48 V, cell size is in m.

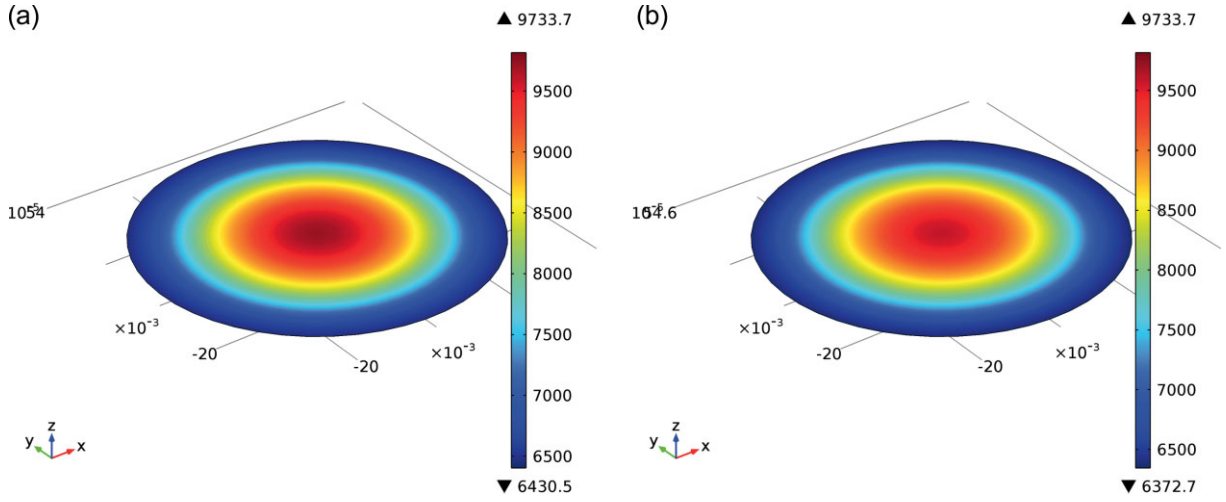

Fig. 5 (a) Current density distribution / A m^{-2} at the anode active area-electrolyte interface at 0.48 V and (b) Current density distribution/A m^{-2} at the electrolyte–cathode active area interface at 0.48 V; cell size is in m.

(the left edge of the graph corresponds to the center of the cell), while Figure 4b shows the potential on the contact surface between electrolyte and cathode.

In agreement with the input parameters, the potential at the anode is uniform and equal to zero outside the active area. Inside the active area, the potential, taken as an absolute value, increases approximately in a linear manner along the thickness direction (Figure 4a).

Now consider Figure 4b: the potential varies also radially; in particular, always considering it in absolute value, it decreases approaching the edges of the cell. In this direction the decrease is lower than along the thickness.

Figure 5 shows the current density distribution on the contact surface between anode active area-electrolyte (Figure 5a) and electrolyte-cathode active area (Figure 5b): it is easily identifiable that current density in this area decreases moving away from the center. This variation is attributable to the difference in concentration of the reactant species inside the cell due to the feeding geometry.

3.3 Mass Flow and Velocity of the Whole System (Channels and Cell)

Figure 6 shows the mass fractions of the present species: mass fraction of the oxygen in the cathode area (Figure 6a) and mass fractions of hydrogen and steam in the anodic area, (Figure 6b and c, respectively). At cathode, input mass fractions are 0.25 for oxygen and 0.75 for nitrogen, while in anode hydrogen mass fraction is 0.73 and steam is 0.27; in the case of oxygen and hydrogen the mass fraction decreases significantly in the edges of the cell due to consumption of the species before reaching these areas. Of course, this influences also the current density generated by electrochemical reactions. The minimum oxygen concentration is located on the outer edges of the channel in contact with the cell, as the oxygen is introduced and diffuses into the cathode and so it gets consumed before reaching the farthest regions. The trend for hydrogen in the anode is similar to that seen for oxygen in the cathode. The minimum amount of hydrogen is located once again on the outer corners of the channel in contact with the cell. This is due to the same reason, namely the diffusion of hydrogen inside the anode and then its consumption. It seems that due to low hydrogen mass flow rate in the inlet channel, and possibly also due to excessive length of the fuel channel and standoff distance [29], hydrogen cannot reach the reaction zone at a sufficient rate. Of course, the reverse trend is found for steam, which is produced by the hydrogen oxidation reaction. This means that where the hydrogen mass fraction decreases, the steam one increases, and the maximum is located on the outer edge of the channel in contact with the cell.

Figure 7 shows the velocity profile in the channels and cell (Figure 7a and b). The velocity in the inlet channel of air is about 0.32 m s^{-1} and in the inlet channel of fuel is about 0.07 m s^{-1}, then drops dramatically inside the electrodes due to the adsorption of species. Near the walls, the speed is lower due to friction.

3.4 Parametric Study

Parametric studies have been performed by changing some effective variables at 1,073 K, 0.48 V, and 400 ml min^{-1} fuel flow rate based on the best fitting condition of the modeling against experimental data. These geometrical and operating properties have been chosen because this model study showed that they have a high effect on the cell performance. The effect of cell radius, cell temperature and electrolyte thickness on polarization curves is shown in Figure 8. For what concerns material properties, several parameters were evaluated: ionic conductivity of the electrolyte, ionic conductivity of anode and cathode functional layers, porosity/permeability of the anode support layer, tortuosity and pore diameter (Figures 9 and 10).

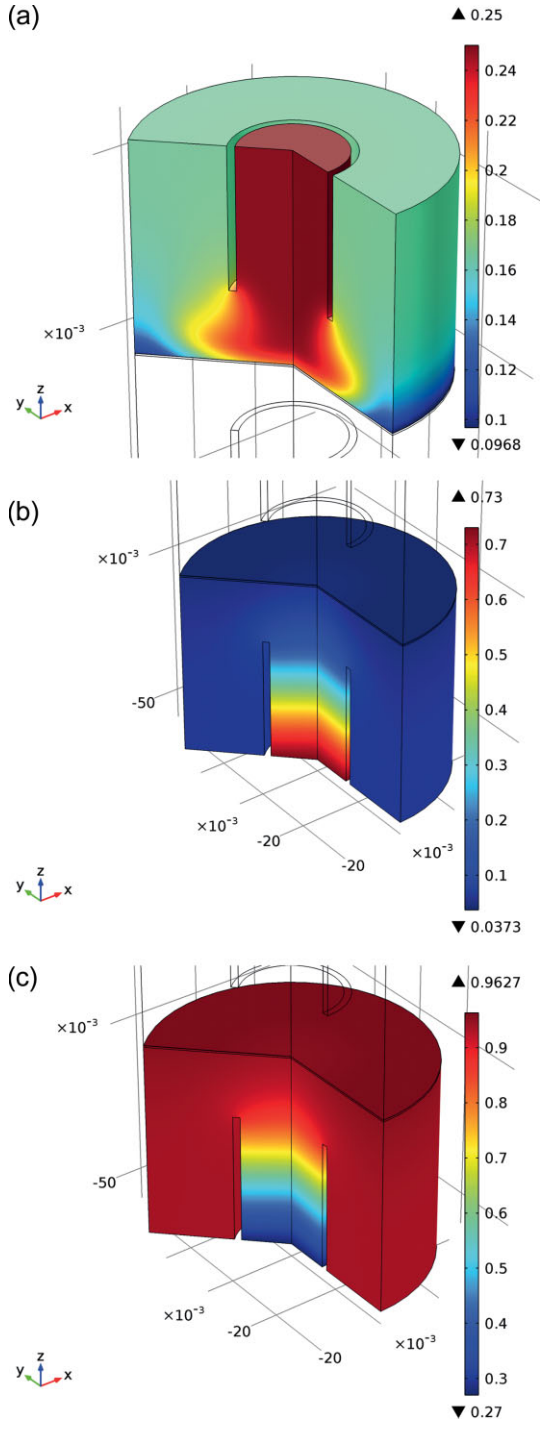

Fig. 6 Mass fractions at 0.48 V of (a) Oxygen in the air channel and cathode area; (b) Hydrogen in the fuel channel and anodic area; (c) Steam in the fuel channel and anodic area; cell size is in m.

Increasing the cell radius with the same fuel and oxidant gas flow has a negative influence on the performance of the cell (Figure 8a). This influence arises from the lower species diffusivity towards the reaction zones in a larger cell with respect to a smaller one.

On the contrary, the effect of increasing the temperature (Figure 8b) is obviously to improve performance, because of the increase in exchange current densities, ionic conductivity and diffusivity. Increasing the temperature has the most significant effect on cell performance.

As expected, an increase in the electrolyte thickness (Figure 8c) leads to worse cell performances due to increased resistance of the electrolyte which in turn affects the overall ohmic cell resistance.

Figures 9 and 10 show the polarization curves obtained from the parametric study on material properties. These material properties have been selected out of many others because an extensive parametric analysis showed that the cell performance is most sensitive to them.

In Figure 9a, the polarization curve simulated with different values of ionic conductivity of the electrolyte are shown. Decreasing the ionic conductivity from 2.26 to 0.56 S m^{-1}, i.e. about four times lower, leads, as expected, to worse cell performances; in particular, the effect of lowering the electrolyte ionic conductivity is to increase the ohmic resistance of the cell, thus influencing the slope of the polarization curve in the medium current density range.

Figure 9b shows the effect of the cathode active layer ionic conductivity on cell performance: decreasing the effective ionic conductivity from 0.81 to 0.41 S m^{-1} (about 50%) diminishes the rate at which reduced oxygen can reach the electrolyte surface. So, a drop in the performance can be expected, and it is actually observed.

Also decreasing the ionic conductivity of the anode functional layer from 0.91 to 0.41 S m^{-1}, i.e. more than 50%, has a negative effect on cell performance (Figure 9c). This output is expected, as a lower effective ionic conductivity negatively affects the transport of oxygen ions species from the electrolyte to the anode active sites.

Increasing porosity from 0.2 to 0.4 (and permeability, as they are interconnected) of the anode support layer (Figure 10a) positively affects the diffusion of species towards the active layer, hence an improvement of performance is expected; nevertheless, this parameter is expected to affect polarization curve in the high current density range, where the fuel utilization factor is higher.

Increasing tortuosity from 2 to 10 (Figure 10b) negatively affects the polarization curves mainly in the region of the limiting current density; in particular, the expected effect is the lowering of the limiting current density as less fuel can reach the active layer, hence a worse cell in comparison with low tortuosity numbers. Decreasing pore diameter from 1 µm to 0.1 µm (Figure 10c) also affects the polarization curve in a negative way. Drastic change in pore diameter has a significant effect on Knudsen diffusion coefficient as Knudsen diffusion is proportional to pore radius.

4 Conclusion

A 2D isothermal axisymmetric model of an anode-supported SOFC has been developed using finite element method. The model has been validated against experimental data in a few different operating conditions, taking care that

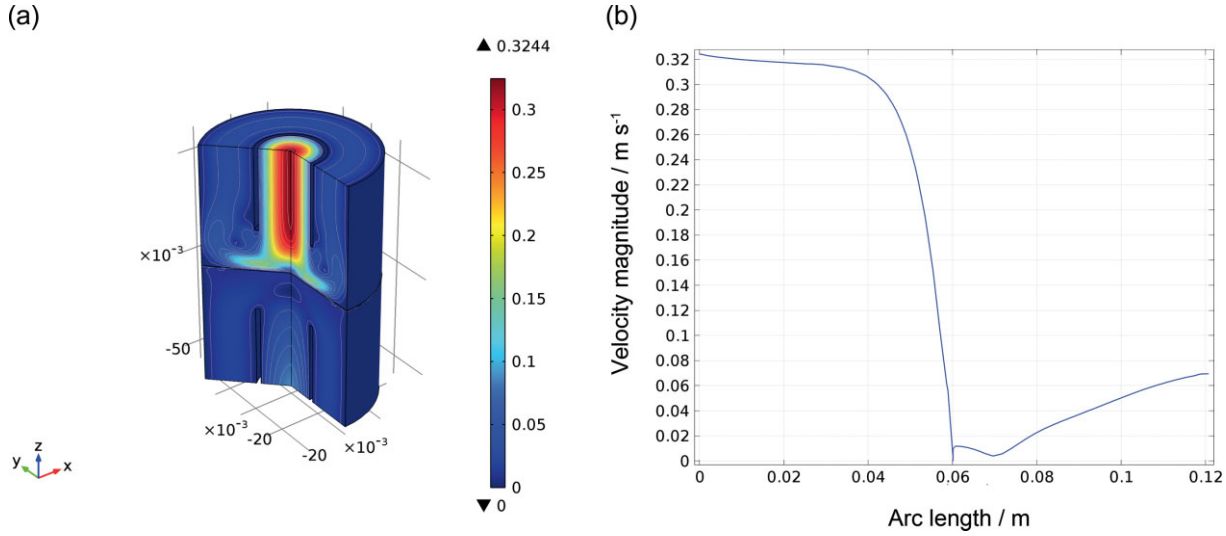

Fig. 7 (a) Velocity profile at 0.48 V of the cell and channels / m s^{-1}; (b) Line graph of velocity magnitude in the cell and channels/ m s^{-1}; cell size is in m.

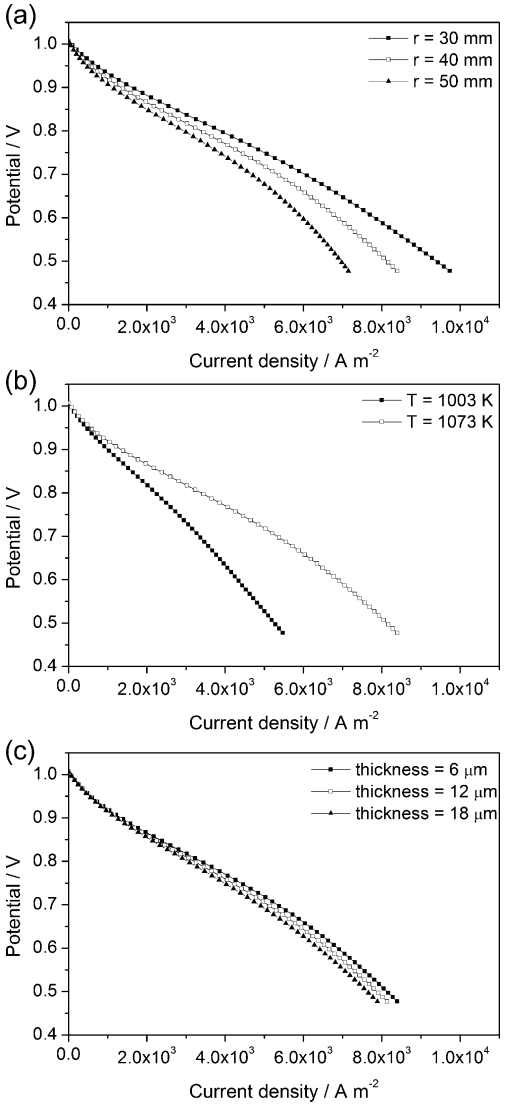

Fig. 8 (a) Influence of the cell radius on the polarization curve ; (b) Influence of the temperature on the polarization curve ; (c) Influence of the electrolyte thickness on the polarization curve.

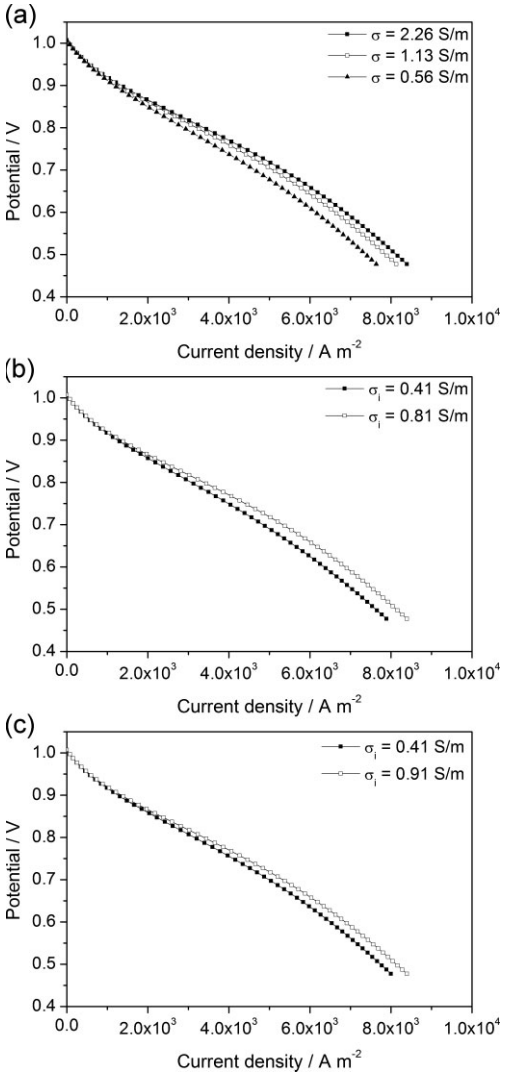

Fig. 9 (a) Influence of the electrolyte conductivity on the polarization curve; (b) Influence of the cathode functional layer effective ionic conductivity on the polarization curve; (c) Influence of the anode functional layer effective ionic conductivity on the polarization curve.

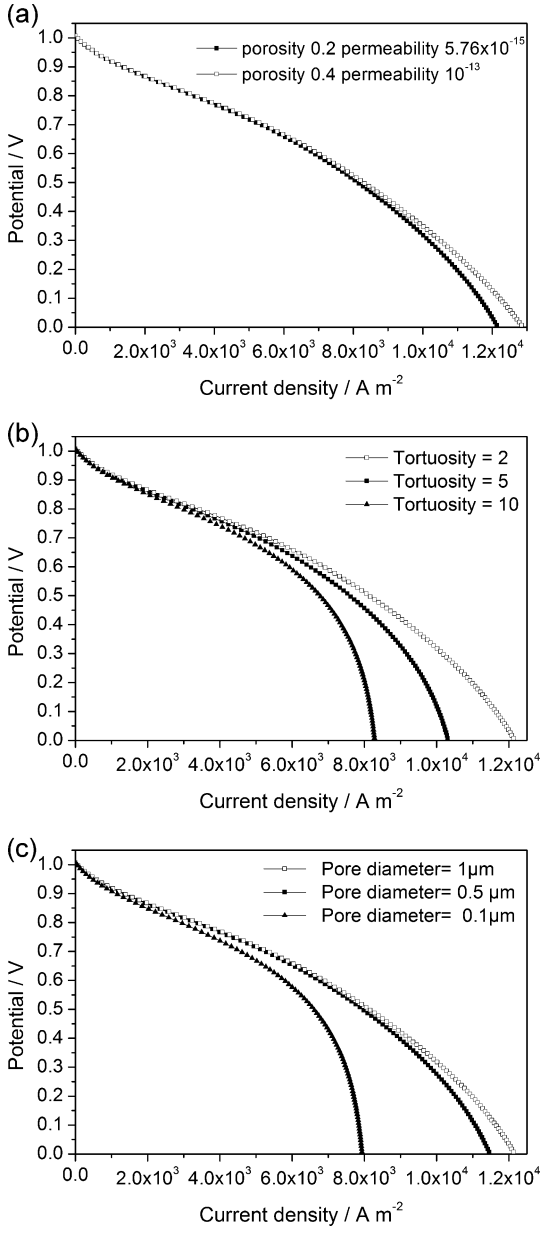

Fig. 10 (a) Influence of the anode support layer porosity/permeability on the polarization curve; (b) Influence of the tortuosity on the polarization curve; (c) Influence of the pore diameter on the polarization curve.

in the simulation, geometrical and chemical–physical (e.g. connected to the materials in use) cell properties as well as operating parameters were the same as those in experiments. Generally, the simulated polarization curves fit quite well the experimental results and this ensures the effectiveness of the model, also considering that no parameter is varied in order to improve fitting. Nevertheless, some discrepancies are observable between modeling and experimental results, particularly in the region of high current density. Low operating temperature (1,003 K) and high fuel stream condition (500 ml min^{-1}) seem to produce the largest discrepancies mostly at high current densities. In view of these results the model has been considered reliable enough to be used in screening optimal cell features, especially with respect to materials properties.

It was then carried out a parametric study on the model to see the influence of effective parameters such as cell temperature, electrolyte thickness, cell radius, and some important material properties: electrolyte conductivity, anode and cathode functional layer effective ionic conductivity, anode support layer porosity/permeability, tortuosity, and pore diameter. Increasing cell radius, electrolyte thickness, and tortuosity have an adverse effect on cell performances; on the contrary, increasing the temperature, conductivities, porosity and pore diameter have a positive effect. In future developments, thermal analysis for bigger cells and short-stacks and also more complex chemical surface reactions using hydrocarbon fuels will be added to the model to expand its versatility.

Acknowledgements

The authors deeply appreciate the fruitful discussions with Dr. Vikram Menon and Prof. Olaf Deutschmann, at Institute for Chemical Technology and Polymer Chemistry, Karlsruhe Institute of Technology "KIT". Also, we sincerely thank the reviewers for their suggestions that led to paper improvement.

Nomenclature

Q_k	general source term in A m^{-3}
k	an index that is *l* for the electrolyte or *s* for the electrode
$i_{0,a}$	anode exchange current density / A m^{-2}
i_a	anode local current density / A m^{-2}
j_a	anode current density per unit volume / A m^{-3}
$a_{v,a}$	anode active specific surface area / m^{-1}
$i_{0,c}$	cathode exchange current density / A m^{-2}
i_c	cathode local current density / A m^{-2}
j_c	cathode current density per unit volume / A m^{-3}
$a_{v,c}$	cathode active specific surface area / m^{-1}
c_{H_2}	molar concentration of hydrogen / mol m^{-3}
c_{H_2O}	molar concentration of steam / mol m^{-3}
$c_{H_2,ref}$	reference (input) concentrations of hydrogen / mol m^{-3}
$c_{H_2O,ref}$	reference (input) concentrations of steam / mol m^{-3}
$c_{O_2,ref}$	reference(input) concentration of oxygen / mol m^{-3}
F	Faraday's constant / C mol^{-1}
R	gas constant / J mol^{-1} K^{-1}
T	temperature / K
P	pressure / Pa
c_t	total molar concentration of species / mol m^{-3}
x_{O_2}	molar fraction of oxygen
u	mass average velocity of the mixture / m s^{-1}
D_{ik}	multi-component effective diffusion coefficient of species *i* and *k* / m^2 s^{-1}
d_{pore}	pore diameter / μm
d_p	particle diameter / μm
D_i^T	thermal diffusion coefficient / kg m^{-1} s^{-1}
R_i	rate expression describing production or consumption of the species

d_k	diffusional driving force acting on species k / m^{-1}
x_k	molar fraction of species k
M	mean molar mass / kg mol^{-1}
V_i,V_j	gases diffusion volumes / m^3 mol^{-1}
g_k	external force (per unit mass) acting on species k / m s^{-2}
u	gas velocity / m s^{-1}

Greek Letters

μ	gas dynamic viscosity / kg m^{-1} s^{-1}
ε	porosity of the layer
τ	tortuosity
κ	permeability / m^2
σ_k	conductivity / S m^{-1}
ϕ	volume fraction of electronic conducting phase in the electrode
$\sigma_{e,eff}$	electronic effective conductivity / S m^{-1}
$\sigma_{i,eff}$	ionic effective conductivity / S m^{-1}
Φ_k	potential / V
η	overvoltage / V
P	mixture density / kg m^{-3}
ω_i	mass fraction of the species in the mixture
ρ	gas density / kg m^{-3}

References

[1] X. Changrong in *Solid Oxide Fuel Cells*, *Vol. 1*, (Eds. J. W. Fergus, R. Hui, X. Li, D. P. Wilkinson, J. Zhang), CRC Press, Boca Raton, FL, USA, **2008**, pp. 1.

[2] R. J. Millington, J. P. Quirk, *Trans. Faraday Soc.* **1961**, *57*, 1200.

[3] T. Ishihara, N. M. Sammes, O. Yamamoto in *High Temperature Solid Oxide Fuel Cells*, *Vol. 4* (Eds. C. S. Subhash, K. Kevin), Elsevier Science, Amsterdam, The Netherlands, **2003**, pp. 83.

[4] Y. Shi, N. Cai, C. Li, *J. Power Sources* **2007**, *164*, 639.

[5] V. M. Janardhanan, O. Deutschmann, *J. Power Sources* **2006**, *162*, 1192.

[6] Y. M. Barzi, A. Raoufi, H. Lari, *Int. J. Hydrogen Energy* **2010**, *35*, 9468.

[7] Y. Xie, X. Xue, *J. Power Sources* **2012**, *209*, 81.

[8] M. Ni, D. Y. C. Leung, M. K. H. Leung, *J. Power Sources* **2008**, *183*, 133.

[9] G. M. Goldin, H. Zhu, R. J. Kee, D. Bierschenk, S. A. Barnett, *J. Power Sources* **2009**, *187*, 123.

[10] I. Zinovik, D. Poulikakos, *Electrochim. Acta* **2009**, *54*, 6234.

[11] A. Lanzini, P. Leone, P. Asinari, *J. Power Sources* **2009**, *194*, 408.

[12] P. Leone, M. Santarelli, P. Asinari, M. Calì, R. Borchiellini, *J. Power Sources* **2008**, *177*, 111.

[13] S. Ubertini, R. Bove, *Modeling Solid Oxide Fuel Cells*, Springer, The Netherlands, **2008**, pp. *51*.

[14] J. Hartvigsen, S. Elangovan, A. Khandkar in *Science and Technology of Zirconia*, *Vol. 5* (Eds. S. P. S. Badwal, M. J. Bannister, R. H. J. Hannink), Technomic Publishing Company Inc., Lancaster, PA, USA, **1993**, pp. 682.

[15] R. Herbin, J. M. Fiard, J. R. Ferguson, *Proc. 1th European Solid Oxide Fuel Cell Forum*, (Eds. U. Bossel), Lucerne, Switzerland, **1994**, pp. 317.

[16] Porous Electrode Documentation, COMSOL 4.3a, **2012**.

[17] H. Zhu, R. J. Kee, *J. Electrochem. Soc.* **2008**, *155*, 715.

[18] A. Pramuanjaroenkij, S. Kakac, X. Y. Zhoua, *Int. J. Hydrogen Energy* **2008**, *33*, 2547.

[19] R. B. Bird, W. E. Stewart, E. N. Lightfoot, *Transport Phenomena,* John-Wiley and Sons, Inc., New York, USA, **1960**.

[20] C. F. Curtiss, R. B. Bird, *Ind. Eng. Chem. Res.* **1999**, *38*, 2515.

[21] R. J. Kee, M. E. Coltrin, P. Glarborg, *Chemically reacting flow: Theory and Practice*, John-Wiley and Sons, Inc., New York, USA, **2003**.

[22] A. Soulaïmani, M. Fortin, *CMAME* **1994**, *118*, 319.

[23] J. A. Wesselingh, R. Krishna, *Mass Transfer in Multicomponent Mixtures*, Delft University Press, The Netherlands, **2000**.

[24] J. Yuan, Y. Huang, B. Sundén, W. G. Wang, *Heat Mass Transfer.* **2009**, *45*, 471.

[25] D. Y. Murzin, T. Salmi, *Catalytic Kinetics*, Elsevier Science, The Netherlands, **2005**.

[26] D. Nield, A. Bejan, *Convection in Porous Media*, Springer, New York, USA, **2006**.

[27] M. L. Bars, M. G. Worster, *J. Fluid Mech.* **2006**, *550*, 149.

[28] J. I. Gazzarri, O. Kesler, *J. Power Sources* **2007**, *167*, 430.

[29] L. A. Chick, K. D. Meinhardt, S. P. Simner, B. W. Kirby, M. R. Powell, N. L. Canfield, *J. Power Sources* **2011**, *196*, 4475.

[30] K. R. Lee, S. H. Choi, J. Kim, H. W. Lee, J. H. Lee, *J. Power Sources* **2005**, *140*, 226.

[31] A. Jena, K. Gupta, *Ceram. Eng. Sci. Proc.* **2005**, *26*, 169.

[32] T. Aloui, K. Halouani, *Appl. Therm. Eng.* **2007**, *27*, 731.

[33] V. M. Janardhanan, V. Heuveline, O. Deutschmann, *J. Power Sources* **2008**, *178*, 368.

[34] J. R. Wilson, W. Kobsiriphat, R. Mendoza, H. Y. Chen, J. M. Hiller, D. J. Miller, K. Thornton, P. W. Voorhees, S. B. Adler, S. A. Barnett, *Nat. Mater.* **2006**, *5*, 541.

[35] R. E. Williford, L. A. Chick, G. D. Maupin, S. P. Simner, J. W. Stevenson, *J. Electrochem. Soc.* **2003**, *150*, 1067.

[36] V. M. Janardhanan, O. Deutschmann, *Electrochim. Acta* **2011**, *56*, 9775.